

Self-Organising Attribute Maps and Pattern Spectra: Novel Explorative Data Analysis Tools for High-Dimensional Vector-Attribute Filtering

Hyoyin Gan, Simon Gazagnes, Mohammad Babai, and Michael H. F. Wilkinson, *Senior Member, IEEE,*

Abstract—Vector-attribute filters are a subset of morphological attribute filters, operating based on connected components of images and are efficient in characterising 2D and 3D images. In this work, we suggest a new general-purpose data-science tool to explore clusters in vector attributes of a component tree, the max-tree, with an unsupervised machine learning technique, self-organising maps (SOMs). The method is applied to a set of (~ 200) medical positron emission tomography (PET) scans used for lung tumour detection. Our results show that certain neurons in the SOM, i.e. clusters of Max-tree nodes, are sensitive to different morphological features in the PET scans, including the lung tumours, especially when the SOM is trained on a significant percentage of high tumour fraction nodes ($>10\%$ of the total nodes). This indicates that the proposed method is promising for exploring morphological features in images without manually thresholding a set of vector attributes.

Index Terms—Component tree, max-tree, mathematical morphology, object detection, algorithms;

1 INTRODUCTION

In mathematical morphology, connected filters are useful tools to preserve particular regions of an image by preserving or removing its connected components (i.e. connected sets of pixels) as a whole [1]–[5]. Attribute filters are an important subset of connected filters [6], which allow filtering based on the size and shape properties of the image. Hierarchical region-based data structures, e.g., component trees, are efficient multi-scale representations of images, allowing efficient implementation of attribute filters. In recent years, attribute filters have been successfully applied in various fields, including the detection of organs and cells in medical images [7], [8], multi-scale analysis in remote sensing [9], [10] and detection of stellar objects in astronomy [11]–[13].

While attribute filters are efficient at extracting individual features when attributes have high discriminative power (i.e., low noise level), they work less efficiently with noisy images where features cannot be discriminated well by a single threshold [14]. When it comes to analysing multiple images of a similar type, it also becomes complicated to compare extracted features between these images. Selecting attributes and setting a dissimilarity threshold, which is a good representation of the given data set, are crucial for the filtering output. These two processes are often done manually [15].

In [16], we introduced a new general-purpose data-

science tool to explore clusters in vector attributes of a component tree, the max-tree, with an unsupervised machine learning technique, self-organising maps (SOMs). In this work, we will study the method further by providing more in-depth theoretical background with an application to medical PET scans. Vector attribute filters are proposed by [17] to improve the performance of traditional attribute filters based on one or more scalar attributes. They enable a better characterisation of objects in an image, in terms of size and shape. Vector attributes can be calculated efficiently from the Max-tree. At the tree-building phase, auxiliary data used for computing the node attributes can be collected and used for calculating attributes.

A major advantage of the new method is that automatic clustering using SOMs takes care of the thresholding of attributes for features in input images. Rather than having to select pairs of attributes for applications like the switchboard platform [18] used in remote sensing, or the 2D pattern spectra computed from max-trees [19] used for diatom classification, we let the system learn an optimal 2D representation from a large collection of attributes. The max-tree is a data structure which enables a computationally efficient implementation of attribute filters [2], [20]–[27].

For clustering of vector attributes, we consider non-linear dimensionality reduction methods to conserve possible non-linear behaviours in the data. Both SOMs [28]–[31] and t-SNE (t-Distributed Stochastic Neighbour Embedding) [32], [33] are popular techniques for projecting high-dimensional data to a 2D map and can be considered for our purposes. t-SNE creates a lower-dimensional embedding by preserving similarity between nearest neighbours (i.e., the local structures). As a result, its similarity function is not sensitive to global structures [32] and the projected distances between clusters are not related to their topology in the original data space [34], [35]. On the other hand, SOMs use the neighbourhood function to define the size

• Hyoyin Gan is with the University of British Columbia, 325 - 6224 Agricultural Road Vancouver, BC V6T 1Z1, Canada. E-mail: hgan@phas.ubc.ca

• Simon Gazagnes is with the University of Texas at Austin, 515 Speedway, Stop C1400, Austin, TX 78712-1205, USA.

• Mohammad Babai and Michael H. F. Wilkinson are with Bernoulli Institute, University of Groningen, 9700 AK Groningen, The Netherlands.

Manuscript received XX XX, XXXX; revised XX XX, XXXX.

of the neighbourhood and determine the extent to which neurons are learning. Therefore, the global structure in the data can be better described when the neighbourhood is appropriately defined. In this work, we will choose SOMs for clustering and reducing data dimensionality.

Similar work is performed by Kiwanuka and Wilkinson in [8], where vector attributes computed from the max-tree were clustered by k-means [36], [37], fuzzy c-means [38] and mean shift clustering [39] to improve the enhancement of objects in medical images. In this work, we extend the idea even further and train vector attributes from max-tree nodes with self-organising maps to automatically detect/classify structures in images and find correlations between extracted structures.

The paper is organised as follows: in Section 2, we introduce a theoretical background with a brief review of the max-tree structure and self-organising maps. In Section 4, we apply the method to medical images and we discuss the results. We conclude in Section 5.

2 THEORETICAL BACKGROUND

In this section, we introduce the concept of the max-tree data structure and self-organising map algorithm.

2.1 Max-tree structure

Connected filters operate on connected components of an image, rather than on the individual pixels by merging flat zones (i.e. a maximal connected region with a constant grey value). Component trees [40] are data structures that organise the connected components from different threshold levels of an image, using the hierarchical parent relationships between nodes. Two variants of these are Min- and Max-trees, first introduced by [2], which are efficient and compact representations of such component trees. In Min-trees the leaves are the regional minima, whereas in Max-trees the leaves represent regional maxima. Min-trees are more suitable for dark structures on a bright background, Max-trees for bright structures on a dark background. Many connected filters can be implemented efficiently via Min- and Max-trees, including (vector-) attribute filters.

Binary images are subsets of a non-empty universal set E and $\mathcal{P}(E)$ is the family of all subsets of E . Grey-scale images I are mapping f from the set E to a subset $T \subseteq \mathbf{R}$, $f : E \rightarrow T$.

A binary operator ψ on a binary image X is considered a *connected operator* if the set difference $X \setminus \psi(X)$ is exclusively composed of connected components of X or its complement X^c . These connected components can be accessed by binary connectivity openings $\Gamma_x(X)$ with a connectivity class $\mathcal{C} \subseteq \mathcal{P}(E)$. A connectivity class \mathcal{C} is a set of all connected component subsets of E [3]. $\Gamma_x(X)$ within X with an intersection point $x \in E$ can be defined as

$$\Gamma_x(X) = \begin{cases} \cup\{C_i \in \mathcal{C} | x \in C_i, C_i \subseteq X\} & \text{if } x \in X \\ \emptyset & \text{otherwise.} \end{cases} \quad (1)$$

In the binary case, attribute filters preserve or remove these connected components C based on some attribute measure

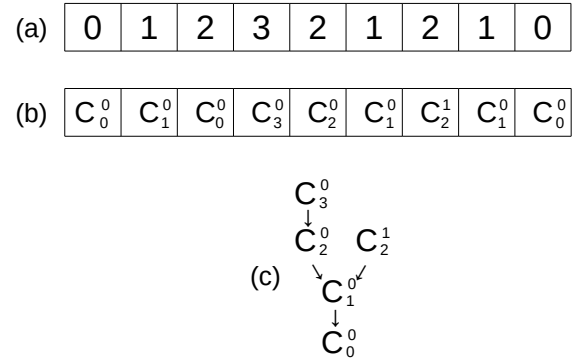


Fig. 1. An example of the max-tree representation with a 1D image $I = [0, 1, 2, 3, 2, 1, 2, 1, 0]$, reproduced from Fig.2 in [45]. (a) Input signal. (b) labelling. (c) Max-tree.

constraints. The constraints Λ are often given by a certain attribute threshold λ ,

$$\Lambda(C) = \text{Attr}(C) \geq \lambda, \quad (2)$$

where $\text{Attr}(C)$ is an attribute of C . For grey-scale images f , a threshold set X_h for connected components with a threshold level h can be defined as

$$X_h(f) = \{x \in E | f(x) \geq h\}. \quad (3)$$

Based on the criterion Λ on connected components, we can define the trivial filter ψ^Λ as

$$\psi^\Lambda(C) = \begin{cases} C & \text{if } \Lambda(C) \text{ is true.} \\ \emptyset & \text{otherwise.} \end{cases} \quad (4)$$

The complete binary attribute filter ψ_Λ with the criterion Λ is defined as

$$\psi_\Lambda(X) = \bigcup_{x \in X} \psi^\Lambda(\Gamma_x(X)). \quad (5)$$

The grey-scale attribute opening ϕ_Λ then can be defined based on the binary opening ψ_Λ as

$$\phi_\Lambda f(x) = \sup\{h \leq f(x) | x \in \psi_\Lambda(X_h(f))\}, \quad (6)$$

where the threshold set has a hierarchy property

$$X_{h+1}(f) \subseteq X_h(f). \quad (7)$$

and this inclusion relationship allows a tree representation, also known as the Max-tree. Images can be efficiently stored by the parent-child relationship at a single point (i.e., the canonical element or level root) between two components A and B when a child A is directly included in its parent B . An example of the max-tree representation for a 1D image $I = [0, 1, 2, 3, 2, 1, 2, 1, 0]$ is shown in Fig.1.

There are three main classes for the max-tree algorithm: immersion algorithms [41], flooding algorithms [2], [23] and merge-based algorithms [42]–[46]. In this work, we use DISCCOFAN (DIStributed Connected COmponent Filtering and ANalysis) [27], [47] to construct the max-tree structure and obtain relevant vector attributes. DISCCOFAN combines and improves the flooding and merging algorithms and is designed to process massive data sets (> 100 gigapixels).

2.2 Vector-attribute filters

Attribute filters discussed above are an important subset of connected filters, introduced by [6]. They are often scalar attribute values, describing the shape and size properties of connected components in an image. Attribute filters work reasonably well when an image has high discriminative power (i.e. low noise) and it has a simple morphological structure. However, the performance becomes worse when the image is noisy and the morphological structure becomes complicated, i.e. the desired structure is not easy to be separated from the image. Vector-attribute filtering was proposed to overcome these drawbacks and improve the description of features in the image.

Traditional attribute filters are often based on one or more scalar attributes such as area, perimeter and elongation. Vector-attribute filters are defined based on the criterion of a distance or dissimilarity measure to a reference vector, obtained by a reference shape.

A multivariate thinning is performed with an attribute threshold vector of dimensionality D . [17] uses a more compact criterion, a dissimilarity measure based on a dissimilarity threshold ϵ , to replace D parameters (in the attribute threshold vector). A multi-variate attribute thinning $\Phi^{\{\Lambda_i\}}(X)$ based on scalar attributes $\{\tau_i\}$ and the corresponding criteria $\{\Lambda_i\}$ with $1 \leq i \leq D$ preserves connected components which satisfy at least one of the criteria $\{\Lambda_i(C)\}$,

$$\Phi^{\{\Lambda_i\}}(X) = \bigcup_{i=1}^D \Phi^{\Lambda_i}(X), \quad (8)$$

where the criteria Λ_i are given as

$$\Lambda_i = \tau_i(C) \geq \lambda_i. \quad (9)$$

The set of scalar attributes and the corresponding attribute thresholds can be written compactly as vectors, such that

$$\vec{\tau} = \{\tau_1, \tau_2, \dots, \tau_D\} \text{ and } \vec{\lambda} = \{\lambda_1, \lambda_2, \dots, \lambda_D\}. \quad (10)$$

A vector attribute thinning requires a criterion:

$$\Lambda_{\vec{\lambda}}^{\vec{\tau}} \equiv \exists i : \tau_i(C) \geq \lambda_i \text{ for } 1 \leq i \leq D. \quad (11)$$

[17] suggests a more compact criterion using a dissimilarity threshold ϵ and a reference vector \vec{r} ,

$$\Lambda_{\vec{r}, \epsilon}^{\vec{\tau}}(C) \equiv d(\tau(\vec{C}), \vec{r}) \geq \epsilon. \quad (12)$$

The vector-attribute thinning $\Phi_{\vec{r}, \epsilon}^{\vec{\tau}}$ of X with respect to a reference vector \vec{r} and using vector-attribute function $\vec{\tau}$ and scalar value ϵ is given by

$$\Phi_{\vec{r}, \epsilon}^{\vec{\tau}}(X) = \{x \in X \mid \Lambda_{\vec{r}, \epsilon}^{\vec{\tau}}(\Gamma_x(X))\}. \quad (13)$$

The dissimilarity measure d quantifies the distance between the reference vector \vec{r} and the vector attribute $\vec{\tau}$ and it can be calculated as the Euclidean distance (e.g., $d(\vec{u}, \vec{v}) = \|\vec{v} - \vec{u}\|$) or other distance measures such as the Mahalanobis distance [17], [48]. Connected components are preserved or removed depending on a dissimilarity to some target shape (for mathematical details, see [8], [19]). Extension to greyscale is straightforward through threshold superposition as in (6).

In this work, to efficiently explore different size and shape structures in 3D medical images, we select a number of vector attributes: the intensity mean, intensity power, intensity variance, X -extent, Y -extent, Z -extent, centre of mass in X , Y and Z .

For size-based attributes, X -extent, Y -extent and Z -extent are selected. They are the differences between the minimum and maximum coordinate values of pixels within each peak component [8], [23].

For shape-based attributes, we consider attributes that are based on image moments [49], such as the centre of centroids in X , Y and Z coordinates. The raw moment of a connected component C of an image $g(x, y)$, is defined as

$$m_{pq} = \sum_{(x,y) \in C} x^p y^q g(x, y), \quad (14)$$

in the two-dimensional space. Mathematically, the raw image moment m_{pqr} of order $(p+q+r)$ for a connected component C of a 3D volume function $V(x, y, z)$ of size $L \times M \times N$ is defined as

$$m_{pqr} = \sum_{(x,y,z) \in C} x^p y^q z^r V(x, y, z), \quad (15)$$

From the raw moment, we can define the centroid, the centre of mass of the intensity, as

$$\{\bar{x}, \bar{y}, \bar{z}\} = \left\{ \frac{M_{100}}{M_{000}}, \frac{M_{010}}{M_{000}}, \frac{M_{001}}{M_{000}} \right\}. \quad (16)$$

and the central moments become, μ_{pqr}

$$\mu_{pqr} = \sum_{x,y,z} V(x, y, z) (x - \bar{x})^p (y - \bar{y})^q (z - \bar{z})^r. \quad (17)$$

We add three additional variables as statistical measures of the image intensity: the intensity mean, variance and power. The intensity power is the sum of the squared difference between the intensity g of a node N and the maximum level of its parents $L(y)$ [12], [13], [50], where $y \in \text{parents}(N)$, defined as

$$\text{power}(N) = \sum_{x \in N} \left(g(x) - \sup_{y \in \text{parents}(N)} L(y) \right)^2. \quad (18)$$

2.3 Pattern Spectra

The multi-scale shape and size description of an image can be summarised by a pattern spectrum [51]. Pattern spectra can be computed from granulometries [52], [53] which are ordered sets of morphological openings or closings. They show how the image content changes as a function of the filter's size or shape parameters [19], [54] and give insight into the distribution of different size and shape classes in an image.

Pattern spectra can be computed efficiently from the Max-tree, as shown in Alg. 1. The Max-tree structure decomposes an image into sets of connected components at different thresholds. The image is then stored as an array of nodes, where a node represents connected components at a threshold. During the construction phase of the tree, at each node, attributes can be computed on the fly and a list of voxels contained is saved for visualisation. Using this information, we can assign attributes (here, the flux

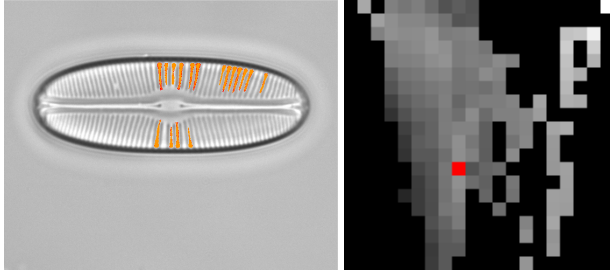


Fig. 2. Diatom image (left) with its 2D size-shape pattern spectrum (right) from [18]. In the image features corresponding to the selected bin in the pattern spectrum are shown in orange.

as an example) at each node to a bin in the 2D pattern spectrum [55].

Fig. 2 shows an example of a 2D size-shape pattern spectrum (right) explored by the switchboard [18] on a diatom image (left). The features corresponding to the selected bin (in red) in the 2D pattern spectra (right) are retrieved to image space, highlighted in orange (left).

Algorithm 1 The MT_pattern_spectrum_2D function

Precondition: The max-tree is stored as an array of nodes `node`. Each node contains an array of attributes `attrib` with a length of at least 2.

`BinFuncAttr1` and `BinFuncAttr2` compute the bins in the spectrum to which a node should be assigned.

```
void MT_pattern_spectrum_2D
    ( MTnode *node,
      greyval **Spectrum) {

    Set all elements of Spectrum to zero

    for all node[i] except root {
        par = node[i].parent;
        flux = (node[i].Gval - node[par].Gval)
            * node[i].area;

        binX = BinFuncAttr1(node[i].attrib[0]);
        binY = BinFuncAttr2(node[i].attrib[1]);

        Spectrum[binX][binY] =
            Spectrum[binX][binY] + flux;
    }
}
```

2.4 Self-organising maps

The nine pre-selected vector attributes are computed from the Max-tree structure built by DISCCOFAN in this work and are then clustered by self-organising maps to explore morphological structures in images.

A self-organising map (SOM) or a Kohonen map, first introduced by Kohonen, is an unsupervised neural network that can project high-dimensional data into a lower-dimensional feature map [28]–[31]. A basic structure of the

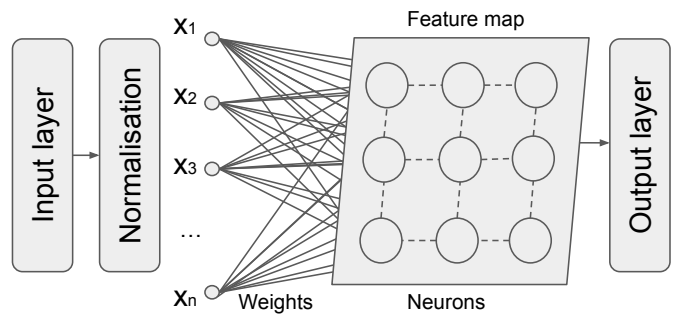


Fig. 3. A basic structure of a self-organising map.

SOM is shown in Fig. 3 and the main idea of the SOM algorithm is presented in Algorithm. 2. SOMs have been successfully applied to problems in various fields including environmental studies [56], sociology [57], economics [58] and agriculture [59], [60]. The SOM typically consists of two layers, an array of input vectors X ,

$$X = [\mathbf{x}_1, \mathbf{x}_2, \dots, \mathbf{x}_n]^T, \quad (19)$$

and an output layer of neurons n_k , where $k = 1, 2, \dots, m$, arranged on a lattice. The input and output layers are fully connected by an array of weight vectors W_k ,

$$W_k = [\mathbf{w}_{1k}, \mathbf{w}_{2k}, \dots, \mathbf{w}_{nk}]^T, \text{ with } k = 1, 2, \dots, m. \quad (20)$$

The learning process of the SOM is as follows: (1) the weight vectors are initialised with random numbers between 0 and 1; (2) the distance d_k between the input vector X and the weight vector W_k is calculated per neuron n_k as

$$d_k = \|X - W_k\| = \sqrt{\sum_{i=1}^m (\mathbf{x}_i - \mathbf{w}_{ik})^2}. \quad (21)$$

(3) find the output neuron with the shortest distance between the input vector and weight vector,

$$c(\mathbf{x}_i) = \arg \min_i \|\mathbf{x}_i - \mathbf{w}_{ik}\|, \quad (22)$$

assign its neuron as the best matching unit (BMU) or the winning neuron in the output layer; (4) calculate and update the topological neighbourhood h_k of the winning neuron. The Gaussian function is a popular choice for the neighbourhood function and it is also used for training SOMs in this work,

$$h_k = \exp \left(- \frac{\|r_k - r_c\|^2}{2\sigma(t)^2} \right), \quad (23)$$

where r_k and r_c are the position vector of the neuron n_k and the BMU, and σ is the neighbourhood spread radius function at iteration t . (5) update the weight vector of each neuron at iteration t ,

$$W_k(t+1) = W_k(t) + \alpha(t)h_k(t)(X - W_k(t)), \quad (24)$$

where $\alpha(t)$ is the learning rate at iteration t . Steps (2)–(5) are repeated until the maximum number of iterations. In this work, we use a minimalistic and NUMPY (Numerical Python)¹ based implementation MINISOM [61] to perform

1. NUMPY is a Python library that performs numerical calculations; <https://numpy.org/>

Data ID	Total nodes	High tumour nodes	High tumour percentage
001	108425	3006	2.77%
002	80430	469	0.58%
003	821235	1607	0.20%
005	168548	85	0.05%
010	92092	1278	1.39%
091	106416	4511	4.24%
192	132020	1336	1.01%
197	120057	1056	0.88%

TABLE 1

Number of nodes and high tumour nodes for example data sets.

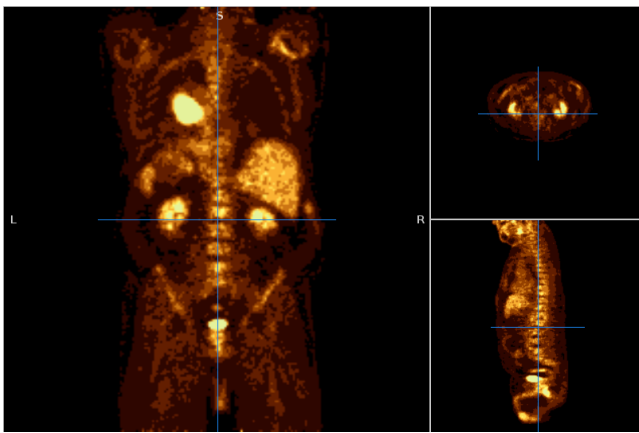


Fig. 4. An example of 3d PET scans from the data set 197 from three different angles (from left, top right and top bottom, corresponding to the coronal, axial and sagittal view).

the SOM algorithm on the data.

Algorithm 2 Main idea of the self-organising map algorithm.

Input: input data vector X ;

Initialisation : weight vectors W_k ;

$N \leftarrow$ Iteration count;

1: **for** $i = 1$ to N **do**

2: $d_k \leftarrow$ the distance between the input and weight vector;

3: $c \leftarrow$ the neuron with the shortest distance to the input (BMU);

4: $b_k \leftarrow$ the topological neighbourhood of the BMU;

5: $W_k(i+1) \leftarrow$ the weight vector of the neuron at iteration i ;

6: **end for**

3 DATA

In this section, we describe two different data sets used for the analysis in this work: (1) fluorodeoxyglucose positron emission tomography (FDG-PET) scans for the detection of lung tumours and (2) satellite images of airports in the Netherlands.

3.1 Fluorodeoxyglucose positron emission tomography (FDG-PET) scans

FDG-PET scans are used to detect metabolically active malignant lesions, stage and monitor the response to therapy of malignant disease [62]. The analysis is based on

Sample	Total nodes	High tumour nodes	High tumour node percentage
1	5000000	10285	0.2%
2	1977900	197790	10.0%
3	988950	197790	20.0%
4	395580	197790	50.0%

TABLE 2
Four different samples used for training SOMs.

~ 200 PET scans with one or two corresponding ground truths (i.e. lung tumour images from PET scans by an expert). The data sets were collected by a multi-centre clinical trial by the ACRIN Cooperative Group (now part of ECOG-ACRIN) and the RTOG Cooperative Group (now part of NRG) using FDG-PET imaging both pre- and post-chemoradiotherapy [63], [64], aiming to study clinical outcome after definitive chemoradiotherapy. Eligible patients were older than 18 years with AJCC-criteria clinical stage IIB/III non-small cell lung carcinoma and were planned for definitive concurrent chemoradiotherapy (inoperable disease). The data are publicly available online via The Cancer Imaging Archive (TCIA) Public Access [65]².

3.2 Pre-processing

The Max-tree data is built for each image by DISCCOFAN. The relevant vector attributes described in section 2 are calculated from the Max-tree data structure. In Table.1, we show details of several example data sets we used for testing. The raw input vector attributes have different units and various magnitudes. To improve the performance of the SOM, the input data X is scaled as follows,

$$X_{\text{scaled}} = \frac{X - X_m}{\sigma_X}, \quad (25)$$

where X_m is the mean of a given data set and σ_X is its standard deviation.

4 RESULTS

4.1 Training self-organising maps

In PET scans, lung tumours typically occupy a small part of each PET scan (< 5%). Nodes with a high tumour fraction (i.e. a node with a tumour volume (> 90%) of the total volume) account only for ~ 0.21% of the total input nodes. Hence, random sampling cannot represent tumour features very well. To solve this problem, we test four different samples for training SOMs including three biased samples with higher fractions of tumour nodes: (1) Randomly sample 5000000 nodes from the combined data sets; (2)-(4) Select all high tumour fraction nodes (197790) and randomly sample from the rest of the nodes that the high tumour nodes account for 10%, 20% and 50% of each sample. The four samples are summarised in Table.2. The parameters we used for training SOMs are summarised in Table.3.

In Fig. 5, we present the trained 10×10 SOMs using the four different samples (from top left to top right) for test data set 197. More examples of SOMs trained on other test

2. <https://wiki.cancerimagingarchive.net/pages/viewpage.action?pageId=39879162>

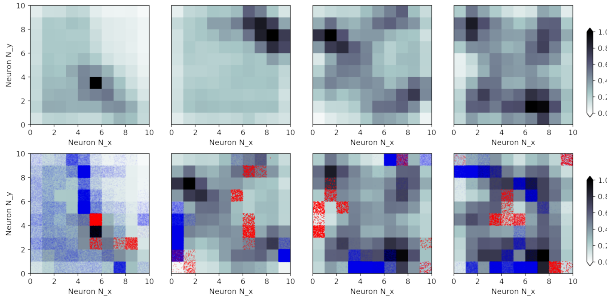


Fig. 5. Top: the 10×10 self-organising maps trained on the four different samples, Sample 1 to 4 (from left to right). Bottom: the distribution of winning neurons from nodes in the data set 197 overlaid on the SOM, nodes with a high tumour fraction are coloured in red and the rest nodes are blue.

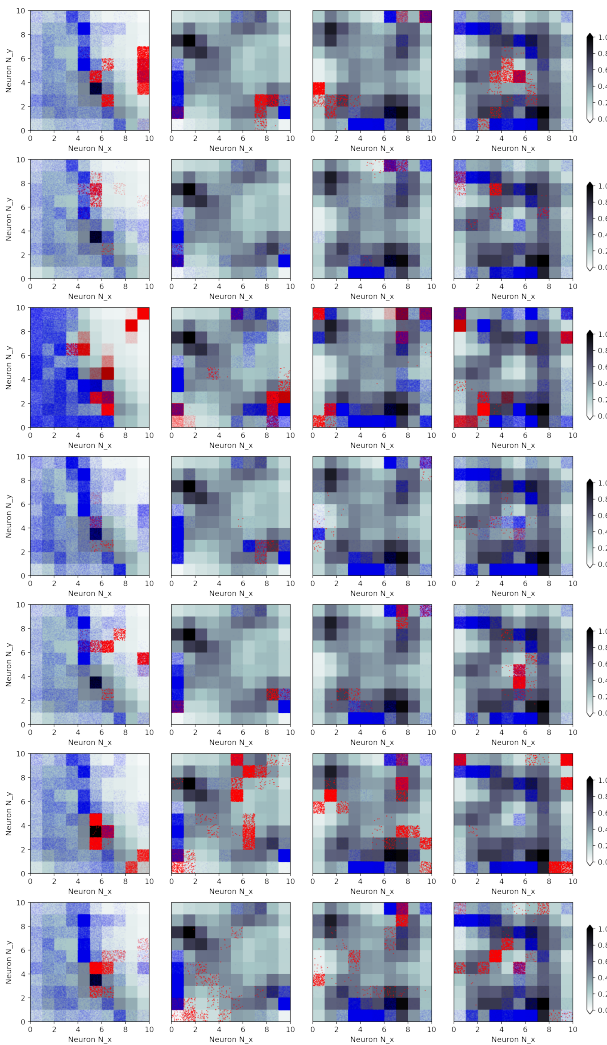


Fig. 6. Self-organising maps trained on the four different samples, Sample 1 to 4 (from left to right), for seven test data sets, from top to bottom, the data set 001, 002, 003, 005, 010, 091 and 192.

Parameter	Value
Map size	10×10
Maximum iteration	100000
Neighbourhood function	Gaussian
Sigma	1.0
Learning rate	0.2
Topology	rectangular
Activation distance	Euclidean

TABLE 3
Parameters used for training a SOM.

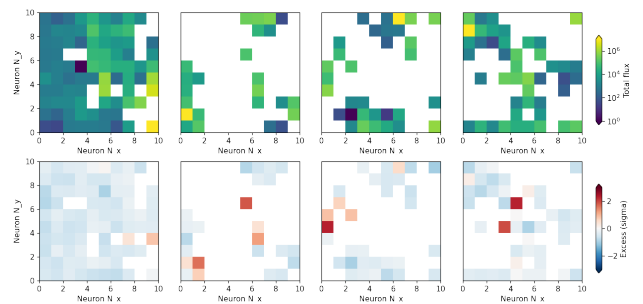


Fig. 7. Top: self-organising pattern spectrum of the data set 197 for the four different samples, Samples 1 to 4 (from left to right). Bottom: normalised excess self-organising pattern spectra of the data set 197 for the four different samples.

sets are provided in Fig. 6. At the bottom, the distribution of winning neurons is shown for each SOM. Using the ground truth, we colour-code the winning neurons with a high tumour fraction. The purpose is to check whether some neurons in the SOMs are sensitive to the lung tumour structures in PET scans. From the results on the test set 197, there exist winning neurons with a high concentration of high tumour fraction nodes ($> 90\%$, coloured in red) in each SOM, which have only a few low-fraction tumour nodes (coloured in blue) and hence can be distinguished from each other. For example, the neuron (5,4) on the bottom left in Fig. 5.

4.2 Self-organising pattern spectra

To explore various morphological features in images, we create a “self-organising pattern spectrum” for per data set and its SOM by summing over node fluxes assigned to each neuron. The results are shown for the data set 197 in Fig. 7 on top. The self-organising pattern spectrum gives us information about neurons containing higher fluxes in the given data set and can be used as a measure of the sensitivity of a neuron to detect features.

For detecting anomalies in images, we create a normalised excess pattern spectrum per data set and its SOM. The self-organising pattern spectra of the entire image sets (~ 200) are combined to obtain the average pattern spectrum and its standard deviation. Using the average pattern spectrum, we calculate the excess response of each pattern spectrum per data set and normalise it by the standard deviation. The normalised excess feature map is shown in Fig. 7 at the bottom for the data set 197. Anomalies in images will appear as an excess for neurons in this map. More examples of self-organising pattern spectra trained on other test sets are provided in Fig. 8.

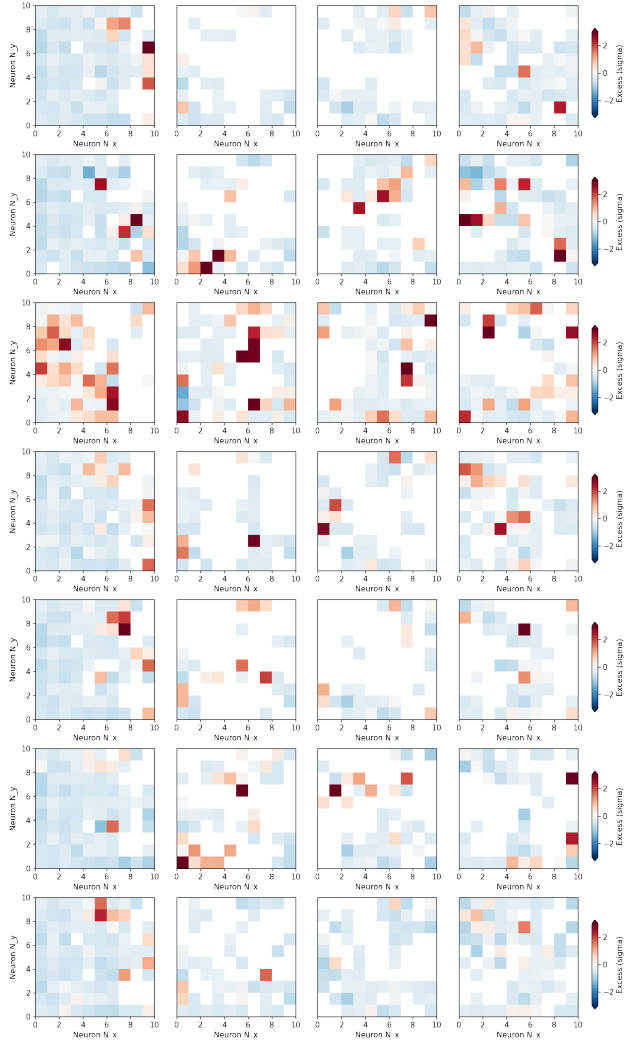


Fig. 8. The normalised excess feature maps of the four different samplings, Sampling 1 to 4 (from left to right), for seven test data sets, from top to bottom, the data set 001, 002, 003, 005, 010, 091 and 192. Neurons with a significant excess response are mapped into the image domain in Figs. 9,10 and 11.

4.3 Filtering based on winning neurons

In this subsection, we perform image filtering based on winning neurons. The purpose is to map vector attribute clusters in the SOM to PET scans and investigate what kind of morphological features each neuron is sensitive to.

In Fig. 9, we compare the ground truth with filtered PET scan 197 based on neurons with a significant excess ($> 1\sigma$) response in the normalised excess feature map in Fig. 7 on the bottom. While the two neurons (7,3) and (9,3) with an excess response in sample 1 are sensitive to anatomical structures (top middle and top right), neurons (1,1), (1,6) and (3,4) (left to right on the bottom) trained respectively by the biased samples 2, 3 and 4 are highly sensitive to the lung tumour and resemble the ground truth (top left). Based on the results, it is likely that SOM neurons trained with added high tumour fraction nodes (using biased samples) are more sensitive to the tumours, on the other hand, SOM neurons are more suitable to detect anomalies in anatomical features if trained on randomly sampled data.

Fig. 10 shows another example of image filtering based

on neurons with an excess response for the data set 002. The total number of nodes in this data set is significantly small compared to the data set 197 (80430 compared to 120057 for the total number of nodes and 469 compared to 1056 for the number of high tumour fraction nodes), this is also partially due to the smaller volume of the tumour in this data set. In this case, SOM neurons with an excess response are not as sensitive to the ground truth as we have seen in the previous example and often, additional structures are detected together with the tumour (top middle and bottom middle). Also, we note that SOM neurons are often sensitive to other organs such as brains, hearts, bladders or kidneys when they have a significantly bright intensity in the PET scan (top right, bottom left and bottom right). More examples of image filtering based on the excess response of SOM neurons are presented in Fig. 11.

From the examples of the two data sets, we note that vector attributes clustered by a SOM can automatically generate neurons that are sensitive to certain shapes and sizes in PET scans, especially some anomalies in the images. By training SOMs on a biased sample, oversampling data having a specific feature that is of interest, one can also create neurons which are more sensitive to this feature, in our case, the lung tumour. Using a biased sample (samples 2, 3 and 4) to train a SOM creates neurons which are more sensitive to the lung tumour in our experiment.

5 CONCLUSION

In this work, we presented a new exploratory tool to analyse morphological features in images by clustering vector attributes with an unsupervised learning method, self-organising maps. The method is applied to medical images for lung tumour detection to explore the possibility of automatic feature detection in the images including lung tumours.

We have shown that neurons in trained SOMs are sensitive to certain features in PET scans, typically organs with high intensity. When trained with a significant number of high-fraction tumour nodes ($> 10\%$ of the total nodes) included in the training set, some neurons are more likely to show an excess response to the lung tumour. These results indicate that the proposed method is a promising exploratory tool for morphological structures in various images.

In future work, we plan to extend the method to explore different types of tree components with other dimensionality-reduction methods. The method can be easily extended to different combinations of data structures such as Alpha-trees [66] and Min-trees with other dimensionality reduction techniques such as Principal Components Analysis (PCA) [67]–[69] for linearly correlated data and Uniform Manifold Approximation and Projection (UMAP) [70] for non-linear cases. Other alternatives include Sharpened Dimensionality Reduction (SDR) [71], and its neural network extension SDR-NNP [72].

Note that t-Distributed Stochastic Neighbour Embedding (t-SNE) algorithm [32], [33] might not be a suitable choice because t-SNE does not preserve global structures in data and the stochastic nature of t-SNE makes the projection results difficult to interpret and replicate as discussed in

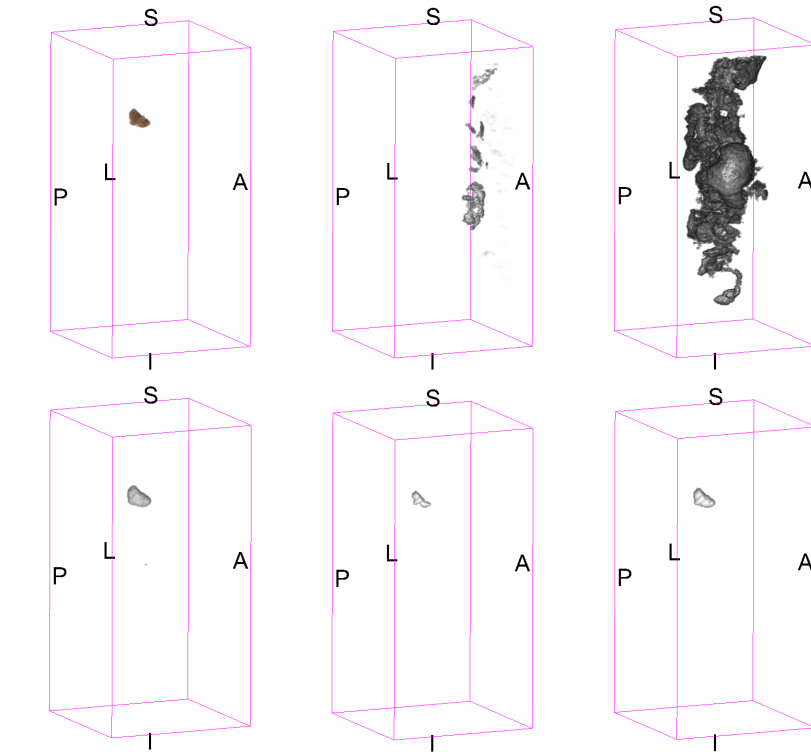


Fig. 9. Comparison of the ground truth and filtered images based on nodes assigned to specific winning neurons showing significant excess signal in the self-organising pattern spectra, for an example data set 197. Top: the ground truth of segmented lung tumour (left) and the PET scan 107 filtered by neuron (7,3) (middle) and neuron (9,3) (right) in the SOM trained on randomly sampled data (sample 1). Bottom: the filtered PET scan 197 based on neuron (1,1) (left) in the SOM trained by the biased sample 2, neuron (1,6) (middle) in the SOM trained by the biased sample 3 and neuron (3,4) (right) in the SOM trained by the biased sample 4.

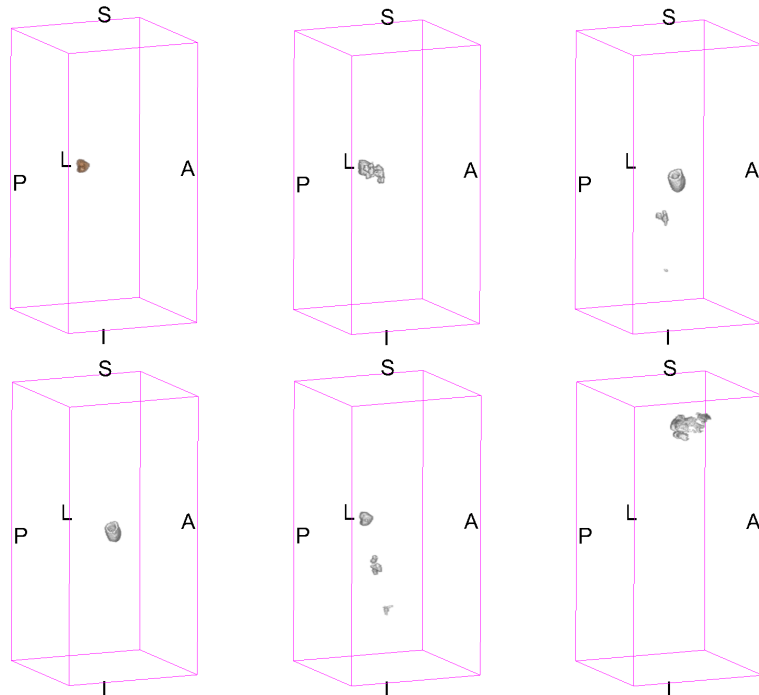


Fig. 10. Comparison of the ground truth and filtered images based on nodes assigned to specific winning neurons showing significant excess signal in the self-organising pattern spectra, for an example data set 002. Top: the ground truth of segmented lung tumour (left) and the PET scan 002 filtered by neuron (7,7) (middle) in the SOM trained on sample 1 and by neuron (2,0) (right) trained on sample 2. Bottom: the filtered PET scan 002 based on neuron (5,1) (left) in the SOM trained by the biased sample 3, neuron (3,7) (middle) and (4,7) (right) in the SOM trained by the biased sample 4.

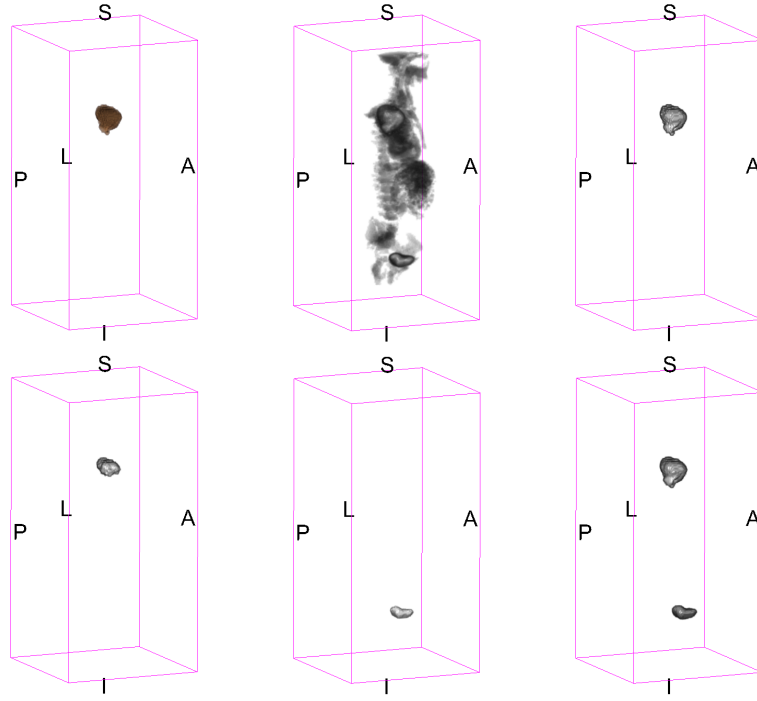


Fig. 11. Comparison of the ground truth and filtered images based on nodes assigned to specific winning neurons, for data set 091. Top: the ground truth of segmented lung tumour (left) and the PET scan 091 filtered by neuron (6,3) (middle) in the SOM trained on sample 1 and by neuron (0,0) (right) trained on sample 2. Bottom: the filtered PET scan 091 based on neuron (1,6) (left) in the SOM trained by the biased sample 3, neuron (9,2) (middle) and (9,7) (right) in the SOM trained by the biased sample 4.

Section 1. Besides, t-SNE cannot handle out-of-sample data, i.e., it cannot map unseen data onto the lower dimensional map. UMAP is one of the leading dimensionality reduction algorithms and performs better at preserving global structure than t-SNE. UMAP is also computationally less expensive for large data sets compared to t-SNE. Depending on the data properties, different sets of vector attributes can be selected. We plan to apply the method to various data sets, including sky images from radio astronomy and data in remote sensing.

One can also consider using spatial pattern spectra [54], [73] as a supplement to ordinary pattern spectra. The extra spatial information might allow us to distinguish more structures in images.

Currently, the implementation of the Self-organising Attribute Maps and Pattern consists of a number of different applications including DISCCOFAN and MINISOM, and the data are exchanged by CSV files. The Python code used for analysis in this work, TREESOM, is publicly available [74]. In the future, we plan to develop a more tightly integrated tool with an intuitive user interface, in analogue to the Switchboard Platform [18] used in remote sensing and make the toolbox publicly available for image analysis.

ACKNOWLEDGMENTS

HG and MHFW would like to acknowledge support from the Centre for Data Science and Systems Complexity (DSSC) at the University of Groningen and a *Marie Skłodowska-Curie COFUND* grant, no.754315.

DATA AVAILABILITY

The FDG-PET data set was provided in collaboration with the American College of Radiology Core Lab and is publicly available online via The Cancer Imaging Archive (TCIA) Public Access [65].

REFERENCES

- [1] P. Salembier and J. Serra, "Flat zones filtering, connected operators, and filters by reconstruction," *IEEE Trans. Image Proc.*, vol. 4, pp. 1153–1160, 1995.
- [2] P. Salembier, A. Oliveras, and L. Garrido, "Antiextensive connected operators for image and sequence processing," *IEEE Transactions on Image Processing*, vol. 7, pp. 555–70, Feb. 1998. DOI: 10.1109/83.663500.
- [3] J. Serra, "Connectivity on complete lattices," *J. Math. Imag. Vis.*, vol. 9, no. 3, pp. 231–251, 1998.
- [4] H. J. A. M. Heijmans, "Connected morphological operators for binary images," *Comp. Vis. Image Understand.*, vol. 73, pp. 99–120, 1999.
- [5] P. Salembier and M. H. F. Wilkinson, "Connected operators: A review of region-based morphological image processing techniques," *IEEE Signal Process. Mag.*, vol. 26, no. 6, pp. 136–157, 2009.
- [6] E. J. Breen and R. Jones, "Attribute openings, thinnings and granulometries," *Comp. Vis. Image Understand.*, vol. 64, no. 3, pp. 377–389, 1996.
- [7] G. K. Ouzounis, S. Giannakopoulos, C. E. Simopoulos, and M. H. F. Wilkinson, "Robust extraction of urinary stones from ct data using attribute filters," in *Proc. Int. Conf. Image Proc. 2009*. IEEE Press, 2009, pp. 2629–2632, ISBN: 9781424456536.
- [8] F. N. Kiwanuka and M. H. F. Wilkinson, "Automatic attribute threshold selection for morphological connected attribute filters," *Pattern recognition*, vol. 53, pp. 59–72, May 2016, ISSN: 0031-3203. DOI: 10.1016/j.patcog.2015.11.012.

- [9] M. H. F. Wilkinson, P. Soille, M. Pesaresi, and G. K. Ouzounis, "Concurrent computation of differential morphological profiles on giga-pixel images," in *Mathematical Morphology and Its Applications to Image and Signal Processing*, P. Soille, M. Pesaresi, and G. Ouzounis, Eds. Springer, 2011, vol. 6671, pp. 331–342, ISBN: 9783642215681.
- [10] G. Cavallaro, M. Dalla Mura, E. Carlinet, T. Géraud, N. Falco, and J. A. Benediktsson, "Region-based classification of remote sensing images with the morphological tree of shapes," in *2016 IEEE International Geoscience and Remote Sensing Symposium (IGARSS)*, 2016, pp. 5087–5090. DOI: 10.1109/IGARSS.2016.7730326.
- [11] C. Berger, T. Géraud, R. Levillain, N. Widynski, A. Baillard, and E. Bertin, "Effective component tree computation with application to pattern recognition in astronomical imaging," vol. 4, pp. IV–41, Jan. 2007. DOI: 10.1109/ICIP.2007.4379949.
- [12] P. Teeninga, U. Moschini, S. C. Trager, and M. H. F. Wilkinson, "Statistical attribute filtering to detect faint extended astronomical sources," *Mathematical Morphology - Theory and Applications*, vol. 1, no. 1, pp. 100–115, Jan. 2016, ISSN: 2353-3390. DOI: 10.1515/mathm-2016-0006.
- [13] C. Haigh, N. Chamba, A. Venhola, et al., "Optimising and comparing source-extraction tools using objective segmentation quality criteria," *Astronomy & Astrophysics*, vol. 645, A107, Jan. 2021. DOI: 10.1051/0004-6361/201936561. [Online]. Available: <https://doi.org/10.1051%2F0004-6361%2F201936561>.
- [14] F. N. Kiwanuka and M. H. F. Wilkinson, "Cluster-based vector-attribute filtering for ct and mri enhancement," in *Proceedings of the 21st International Conference on Pattern Recognition, ICPR 2012*, IEEE, 2012, pp. 3112–3115, ISBN: 978-4-9906441-0-9. [Online]. Available: <http://www.icpr2012.org/>.
- [15] Y. Gavet, M. Fernandes, J. Debayle, and J.-C. Pinoli, "Dissimilarity criteria and their comparison for quantitative evaluation of image segmentation: application to human retina vessels," *Machine Vision and Applications*, vol. 25, no. 8, pp. 1953–1966, 2014. DOI: 10.1007/s00138-014-0625-2. [Online]. Available: <https://hal.archives-ouvertes.fr/hal-01094137>.
- [16] H. Gan and M. H. F. Wilkinson, "Self-organising attribute maps and pattern spectra for image exploration," in *Proc. DGMM 2023*, submitted, 2023.
- [17] E. R. Urbach, N. J. Boersma, and M. H. F. Wilkinson, "Vector-attribute filters," in *Mathematical Morphology: 40 Years On*, C. Ronse, L. Najman, and E. Decencière, Eds., Dordrecht: Springer Netherlands, 2005, pp. 95–104, ISBN: 978-1-4020-3443-5.
- [18] G. Ouzounis, V. Syrris, L. Gueguen, and P. Soille, "The switchboard platform for interactive image information mining," in *Proceedings of 8th conference on image information mining, ESA-EUSIC-JRC, Joint Research Centre of the European Commission*, 2012.
- [19] E. R. Urbach, J. B. T. M. Roerdink, and M. H. F. Wilkinson, "Connected shape-size pattern spectra for rotation and scale-invariant classification of gray-scale images," *IEEE Transactions on Pattern Analysis and Machine Intelligence*, vol. 29, no. 2, pp. 272–285, 2007. DOI: 10.1109/TPAMI.2007.28.
- [20] I. Purnama, M. Wilkinson, A. Veldhuizen, et al., "Branches filtering approach for max-tree," in *VISAPP (1)*, Jan. 2007, pp. 328–332.
- [21] M. A. Westenberg, J. B. T. M. Roerdink, and M. H. F. Wilkinson, "Volumetric attribute filtering and interactive visualization using the max-tree representation," *IEEE Transactions on Image Processing*, vol. 16, pp. 2943–52, Jan. 2008. DOI: 10.1109/TIP.2007.909317.
- [22] A. Ananda, I. Purnama, and M. Hery Purnomo, "Ct lung image filtering based on max-tree method," in *2011 2nd International Conference on Instrumentation, Communications, Information Technology, and Biomedical Engineering*, Nov. 2011, pp. 137–140. DOI: 10.1109/ICICI-BME.2011.6108611.
- [23] M. H. F. Wilkinson, "A fast component-tree algorithm for high dynamic-range images and second generation connectivity," in *Proceedings - International Conference on Image Processing, ICIP*, Sep. 2011, pp. 1021–1024. DOI: 10.1109/ICIP.2011.6115597.
- [24] L. Tavares, R. Souza, L. Rittner, R. Machado, and R. Lotufo, "A max-tree simplification proposal and applications for the interactive max-tree visualization tool," Oct. 2016, pp. 313–320. DOI: 10.1109/SIBGRAPI.2016.050.
- [25] F. Guiotte, S. Lefèvre, and T. Corpetti, "Attribute filtering of urban point clouds using max-tree on voxel data," in *Proc. Int. Symp. Math. Morphology (ISMM) 2019*, May 2019, pp. 391–402.
- [26] R. Tao and Y. Song, "An automatic traffic peak picking method based on max tree," in *2020 IEEE 5th International Conference on Intelligent Transportation Engineering (ICITE)*, Sep. 2020, pp. 88–92. DOI: 10.1109/ICITE50838.2020.9231459.
- [27] S. Gazagnes and M. H. F. Wilkinson, "Distributed connected component filtering and analysis in 2-d and 3-d tera-scale data sets," *IEEE Trans. Image Proc.*, vol. 30, pp. 3664–3675, 2021, ISSN: 1057-7149. DOI: 10.1109/TIP.2021.3064223.
- [28] T. Kohonen, "Self-organized formation of topologically correct feature maps," *Biological cybernetics*, vol. 43, no. 1, pp. 59–69, 1982.
- [29] T. Kohonen, "The self-organizing map," *Proceedings of the IEEE*, vol. 78, no. 9, pp. 1464–1480, 1990. DOI: 10.1109/5.58325.
- [30] *Self-organizing maps*, 3rd, ser. Springer series in information sciences, 30. Springer, Dec. 2001, ISBN: 978-3-540-67921-9. [Online]. Available: <http://www.worldcat.org/isbn/3540679219>.
- [31] D. Miljković, "Brief review of self-organizing maps," in *2017 40th International Convention on Information and Communication Technology, Electronics and Microelectronics (MIPRO)*, 2017, pp. 1061–1066. DOI: 10.23919/MIPRO.2017.7973581.
- [32] L. Van der Maaten and G. Hinton, "Visualizing data using t-sne," *Journal of machine learning research*, vol. 9, no. 11, 2008.
- [33] L. Van Der Maaten, "Accelerating t-sne using tree-based algorithms," *The Journal of Machine Learning Research*, vol. 15, no. 1, pp. 3221–3245, 2014.
- [34] M. Wattenberg, F. Viégas, and I. Johnson, "How to use t-sne effectively," *Distill*, vol. 1, no. 10, e2, 2016.
- [35] Y. Zhou and T. O. Sharpee, "Using global t-sne to preserve intercluster data structure," *Neural Computation*, vol. 34, no. 8, pp. 1637–1651, 2022.
- [36] J. MacQueen, "Classification and analysis of multivariate observations," in *5th Berkeley Symp. Math. Statist. Probability*, 1967, pp. 281–297.
- [37] S. Lloyd, "Least squares quantization in pcm," *IEEE transactions on information theory*, vol. 28, no. 2, pp. 129–137, 1982.
- [38] J. C. Bezdek, R. Ehrlich, and W. Full, "Fcm: The fuzzy c-means clustering algorithm," *Computers & Geosciences*, vol. 10, no. 2, pp. 191–203, 1984, ISSN: 0098-3004. DOI: [https://doi.org/10.1016/0098-3004\(84\)90020-7](https://doi.org/10.1016/0098-3004(84)90020-7). [Online]. Available: <https://www.sciencedirect.com/science/article/pii/0098300484900207>.
- [39] K. Fukunaga and L. Hostetler, "The estimation of the gradient of a density function, with applications in pattern recognition," *IEEE Transactions on information theory*, vol. 21, no. 1, pp. 32–40, 1975.
- [40] R. Jones, "Connected filtering and segmentation using component trees," *Computer Vision and Image Understanding*, vol. 75, no. 3, pp. 215–228, 1999, ISSN: 1077-3142. DOI: <https://doi.org/10.1006/cviu.1999.0777>. [Online]. Available: <https://www.sciencedirect.com/science/article/pii/S1077314299907774>.
- [41] R. Tarjan, "Efficiency of a good but not linear set union algorithm," *J. ACM*, vol. 22, pp. 215–225, Apr. 1975. DOI: 10.1145/321879.321884.
- [42] D. Menotti, L. Najman, A. De, and A. Araújo, "1d component tree in linear time and space and its application to gray-level image multithresholding," in *Proc. Int. Symp. Math. Morphology (ISMM) 2007*, vol. 1, Nov. 2007, pp. 437–448.
- [43] G. K. Ouzounis and M. H. F. Wilkinson, "A parallel implementation of the dual-input max-tree algorithm for attribute filtering," in *Proc. Int. Symp. Math. Morphology (ISMM) 2007*, vol. 1, Oct. 2007, pp. 449–460.
- [44] P. Matas, E. Dokladalova, M. Akil, et al., "Parallel algorithm for concurrent computation of connected component tree," vol. 5259, Oct. 2008, pp. 230–241, ISBN: 978-3-540-88457-6. DOI: 10.1007/978-3-540-88458-3_21.
- [45] M. H. F. Wilkinson, H. Gao, W. Hesslink, J.-E. Jonker, and A. Meijster, "Concurrent computation of attribute filters on shared memory parallel machines," *IEEE Transactions on Pattern Analysis and Machine Intelligence*, vol. 30, pp. 1800–13, Nov. 2008. DOI: 10.1109/TPAMI.2007.70836.
- [46] V. Morard, P. Dokladal, and E. Decencière, "One-dimensional openings, granulometries and component trees in o(1) per pixel," *IEEE Journal of Selected Topics in Signal Processing*, vol. 6, pp. 840–848, Nov. 2012. DOI: 10.1109/JSTSP.2012.2201694.
- [47] S. Gazagnes and M. H. F. Wilkinson, "Distributed component forests in 2-d: Hierarchical image representations suitable for tera-scale images," *International Journal of Pattern Recognition and Artificial Intelligence*, vol. 33, no. 11 SI, Oct. 2019, ISSN: 0218-0014. DOI: 10.1142/S0218001419400123.
- [48] B. Naegel, N. Passat, N. Boch, and M. Kocher, "Segmentation using vector-attribute filters: Methodology and application to

- dermatological imaging," *ISMM 2007, 8th International Symposium on Mathematical Morphology*, vol. 1, Oct. 2007.
- [49] M.-K. Hu, "Visual pattern recognition by moment invariants," *IRE Trans. Inf. Theory*, vol. 8, pp. 179–187, 1962.
- [50] T. X. Nguyen, G. Chierchia, L. Najman, *et al.*, "Cgo: Multiband astronomical source detection with component-graphs," in *2020 IEEE International Conference on Image Processing (ICIP)*, 2020, pp. 16–20. DOI: 10.1109/ICIP40778.2020.9191276.
- [51] P. Maragos, "Pattern spectrum and multiscale shape representation," *IEEE Transactions on Pattern Analysis and Machine Intelligence*, vol. 11, no. 7, pp. 701–716, 1989. DOI: 10.1109/34.192465.
- [52] G. Matheron, "Éléments pour une théorie des milieux poreux," 1967.
- [53] L. Vincent, "Granulometries and opening trees," *Fundam. Inform.*, vol. 41, pp. 57–90, Jan. 2000. DOI: 10.3233/FI-2000-411203.
- [54] M. H. F. Wilkinson, "Generalized pattern spectra sensitive to spatial information," in *2002 International Conference on Pattern Recognition*, IEEE, vol. 1, 2002, pp. 21–24.
- [55] U. Moschini, "Efficient morphological tools for astronomical image processing," English, Ph.D. dissertation, University of Groningen, 2016, ISBN: 978-90-367-8848-9.
- [56] R. Xiao, R. Cui, M. Lin, L. Chen, Y. Ni, and X. Lin, "Somdnnd: Image change detection based on self-organizing maps and deep neural networks," *IEEE Access*, vol. 6, pp. 35 915–35 925, 2018. DOI: 10.1109/ACCESS.2018.2849110.
- [57] N. Sapkota, W. Karwowski, and T. Ahram, "Application of evolving self-organizing maps for analysis of human adverse events in the context of complex socioeconomic infrastructure interactions," *IEEE Transactions on Human-Machine Systems*, vol. 45, no. 4, pp. 500–509, 2015. DOI: 10.1109/THMS.2015.2412120.
- [58] A. Alshanti and A. Rasheed, "Self-organising map based framework for investigating accounts suspected of money laundering," *Frontiers in Artificial Intelligence*, vol. 4, 2021, ISSN: 2624-8212. DOI: 10.3389/frai.2021.761925. [Online]. Available: <https://www.frontiersin.org/article/10.3389/frai.2021.761925>.
- [59] J. Cirera, J. A. Carino, D. Zurita, and J. A. Ortega, "Data analytics for performance evaluation under uncertainties applied to an industrial refrigeration plant," *IEEE Access*, vol. 7, pp. 64 127–64 135, 2019. DOI: 10.1109/ACCESS.2019.2917079.
- [60] M. Haggag, S. Abdelhay, A. Mecheter, S. Gowid, F. Musharavati, and S. Ghani, "An intelligent hybrid experimental-based deep learning algorithm for tomato-sorting controllers," *IEEE Access*, vol. 7, pp. 106 890–106 898, 2019. DOI: 10.1109/ACCESS.2019.2932730.
- [61] G. Vettigli, *Minisom: Minimalistic and numpy-based implementation of the self organizing map*, 2018. [Online]. Available: <https://github.com/JustGlowing/minisom/>.
- [62] S. Tsim, C. O'dowd, R. Milroy, and S. Davidson, "Staging of non-small cell lung cancer (nsclc): A review," *Respiratory medicine*, vol. 104, no. 12, pp. 1767–1774, 2010.
- [63] K. Clark, B. Vendt, K. Smith, *et al.*, "The cancer imaging archive (tcia): Maintaining and operating a public information repository," *Journal of digital imaging*, vol. 26, no. 6, pp. 1045–1057, 2013.
- [64] M. Machta, F. Duan, B. A. Siegel, *et al.*, "Prediction of survival by [18f] fluorodeoxyglucose positron emission tomography in patients with locally advanced non-small-cell lung cancer undergoing definitive chemoradiation therapy: Results of the acrin 6668/rtog 0235 trial," *Journal of clinical oncology*, vol. 31, no. 30, p. 3823, 2013.
- [65] P. Kinahan, M. Muzi, B. Bialecki, B. Herman, and L. Coombs, "Data from the acrin 6668 trial nsclc-fdg-pet," *Cancer Imaging Arch*, vol. 10, 2019.
- [66] G. K. Ouzounis and P. Soille, *The Alpha-Tree algorithm*. Publications Office of the European Union, Dec. 2012, ISBN: 978-92-7926279-1. DOI: 10.2788/48773.
- [67] L. Sirovich and M. Kirby, "Low-dimensional procedure for the characterization of human faces," *Josa a*, vol. 4, no. 3, pp. 519–524, 1987.
- [68] M. Kirby and L. Sirovich, "Application of the kl procedure for the characterization of human faces," *IEEE Trans. Pattern Anal. Mach. Intell*, vol. 98, no. 6, pp. 1031–1044, 2010.
- [69] A. Daffertshofer, C. J. Lamoth, O. G. Meijer, and P. J. Beek, "Pca in studying coordination and variability: A tutorial," *Clinical biomechanics*, vol. 19, no. 4, pp. 415–428, 2004.
- [70] L. McInnes, J. Healy, and J. Melville, "Umap: Uniform manifold approximation and projection for dimension reduction," *arXiv preprint arXiv:1802.03426*, 2018.
- [71] Y. Kim, A. C. Telea, S. C. Trager, and J. B. Roerdink, "Visual cluster separation using high-dimensional sharpened dimensionality reduction," *Information Visualization*, vol. 21, no. 3, pp. 197–219, 2022. DOI: 10.1177/14738716221086589. eprint: <https://doi.org/10.1177/14738716221086589>. [Online]. Available: <https://doi.org/10.1177/14738716221086589>.
- [72] Y. Kim, M. Espadoto, S. Trager, J. B. Roerdink, and A. Telea, "Sdr-nnp: Sharpened dimensionality reduction with neural networks," in *Proceedings of the 17th International Joint Conference on Computer Vision, Imaging and Computer Graphics Theory and Applications*, SciTePress, 2022, pp. 63–76.
- [73] S. Land and M. H. F. Wilkinson, "A comparison of spatial pattern spectra," in *International Symposium on Mathematical Morphology and Its Applications to Signal and Image Processing*, Springer, 2009, pp. 92–103.
- [74] H. Gan, *Self-organising attribute maps and pattern spectra*, 2023. [Online]. Available: <https://github.com/hgan0/tree-SOM/>.

Hyoyin Gan obtained an MSc in physics from Heidelberg University in 2017 with the thesis "Nuclear reactions in astrophysical plasmas" at Max-Planck Institute for nuclear physics. After that, she joined the LOFAR-EoR (Low Frequency Array Epoch of Reionisation) team at Kapteyn Institute and the Centre for Data Science and Systems Complexity of the University of Groningen and obtained a PhD in 2022. Currently, she is a postdoctoral research fellow in 21 cm cosmology working on CHIME (The Canadian Hydrogen Intensity Mapping Experiment) data analysis and map-making pipeline at the University of British Columbia. Her research focuses on the calibration and analysis of data from radio interferometers such as LOFAR and CHIME, using various techniques including statistical methods, image processing and machine learning.

Simon Gazagnes obtained the B.S and M.S degrees in electrical engineering and signal and image processing from the National Institute of Applied Sciences of Lyon (France) in 2016, and first worked on biological imaging with the MORPHEME team in Sophia Antipolis. In 2017, he received an MSc degree in astrophysics from the University of Toulouse (France) and joined the STARBURST team in the Geneva Observatory to work on modeling and data analysis of galaxy spectroscopic observations. He did his PhD with the Centre for Data Science and Systems Complexity of the University of Groningen, developing efficient methods based on connected morphology to meet the needs of astrophysical and particle physics applications. He is currently postdoctoral researcher at the University of Texas at Austin.

M. Babai obtained an MSc in computing science from the Institute of Mathematics and computing science, University of Groningen, after which he worked on developing machine-learning based tools for subatomic particle identification at Kernfysisch Versneller Instituut (KVI), University of Groningen. He obtained a PhD at Bernoulli Institute for Mathematics, Computer Science and AI at University of Groningen. He is currently working at Center for Information Technology (CIT), University of Groningen, as a scientific-programmer/data-scientist. He is interested in morphological image analysis and graph morphology and also in application and development of data-science techniques for large scale data-processing.

Michael H. F. Wilkinson obtained an MSc in astronomy from the Kapteyn Astronomical Institute, University of Groningen in 1993, after which he worked on image analysis of intestinal bacteria at the Department of Medical Microbiology, University of Groningen, obtaining a PhD at the Institute of Mathematics and Computing Science, also in Groningen, in 1995. He was appointed as researcher at the Centre for High Performance Computing in Groningen working on simulating the intestinal microbial ecosystem on parallel computers. After this, he worked as a researcher at the Johann Bernoulli Institute for Mathematics and Computer Science on image analysis of diatoms. He is currently associate professor at the Bernoulli Institute for Mathematics, Computer Science and Artificial Intelligence, working on morphological image analysis and especially connected morphology and models of perceptual grouping. An important research focus is on handling giga- and tera-scale images in remote sensing, astronomy and other digital imaging modalities.